PCCP

PAPER

View Article Online
View Journal | View Issue

Cite this: *Phys. Chem. Chem. Phys.*, 2018, **20**, 14725

Modelling the atomic arrangement of amorphous 2D silica: a network analysis†

Projesh Kumar Roy, [ab] Markus Heyde [c] and Andreas Heuer *[b]

Received 27th February 2018,
Accepted 8th May 2018

DOI: 10.1039/c8cp01313f

rsc.li/pccp

The recent experimental discovery of a semi two-dimensional silica glass has offered a realistic description of the random network theory of a silica glass structure, initially discussed by Zachariasen. To study the structure formation of silica in two dimensions, we introduce a two-body force field, based on a soft core Yukawa potential. The different configurations, sampled *via* Molecular dynamics simulations, can be directly compared with the experimental structures, which have been provided in the literature. The parameters of the force field are obtained from comparison of the nearest-neighbor distances between experiment and simulation. Further key properties such as angle distributions, distribution of ring sizes and triplets of rings are analyzed and compared with the experiment. Of particular interest is the spatial correlation of ring sizes. In general, we observe a very good agreement between experiment and simulation. Additional insight from the simulations is provided about the temporal and spatial stability of the rings in dependence of their size.

1 Introduction

The atomistic arrangement of glassy materials is often described by the continuous random network model.[1] Silica is by far the most commonly used and extensively studied oxide-glass material. More than 80 years ago, Zachariasen began the search for a theory to explain the structure of amorphous materials.[2] For reasons of simplicity, the ideas of the random network theory were formulated in 2D. Conceptually, this model can be applied to silica, when silicon atoms are reduced to three rather than four oxygen neighbors as in bulk silica. Experimentally, neutron diffraction (ND) and X-ray diffraction (XRD) studies were the only useful methods available to peek into the complex world of glass structures. However, due to the integrating nature of these methods,[3] an experimental all-atom understanding of the structure of silica glass remained impossible. The Bell and Dean wire-frame model[4] or the Shackelford tile model[5] were some of the famous attempts to understand random network theory of silica by mechanical models. Development of computer simulations has helped us to understand the properties of silica networks more deeply. Empirical force-fields like the Beest–Kramer–Santen (BKS) potential[6] or the Tangney–Scandolo (TS) potential[7] are now well established for simulating the bulk silica network. A comparison of these model force-fields can be found in ref. 8.

1.1 Experimental background: two-dimensional silica

The hand-drawn two-dimensional model of Zachariasen became reality only recently through the experiments of Lichtenstein *et al.*[9] and Huang *et al.*[10] It was possible to prepare an extremely thin silica film on Ru(0001)[9] as well as on graphene.[10] The 'two-dimensional silica' is indeed a 'semi 2D' allotrope of silica, that fulfills all valence criteria of silicon and oxygen in 3D, but still maintains a flat surface at reduced dimensionality.

The surface was studied mainly using a scanning tunneling microscopy (STM) and for the first time a detailed real space image of a silica network was obtained. Depending on the initial film coverage, annealing temperature and cooling methods,[11] the surface of two dimensional silica could either show amorphous or crystalline network structures. Despite having a flat surface, it was not possible to capture both silicon and oxygen coordinates at the same time with STM because of their different chemical properties. The authors had to make some assumption with the backing of density function theory (DFT) calculations to estimate the positions of one component, given the exact positions of the

[a] *NRW Graduate School of Chemistry, Wilhelm-Klemm-Str. 10, 48149 Münster, Germany*
[b] *Institut für Physikalische Chemie, Westfälische Wilhelms-Universität Münster, Corrensstr. 28/30, 48149 Münster, Germany. E-mail: andheuer@uni-muenster.de; Fax: +49-251-83-29159; Tel: +49-251-83-29177*
[c] *Fritz-Haber-Institut der Max-Planck-Gesellschaft, Faradayweg 4-6, 14195 Berlin, Germany*

† Electronic supplementary information (ESI) available: (i) discussion of the absolute units of the model, (ii) finite size effect, (iii) the comparison of the pair distribution functions of the unconvoluted simulation data as compared to the two different experimental sets of data, based on oxygen or silicon reconstruction, (iv) the precise values of the ring distribution for the experimental and simulation data, including the statistical errors, (v) detailed probabilities of all observed doublets and triplets for the experimental and simulation data, (vi) sample coordinates for 500 particle simulated structure and experimental structure. See DOI: 10.1039/c8cp01313f

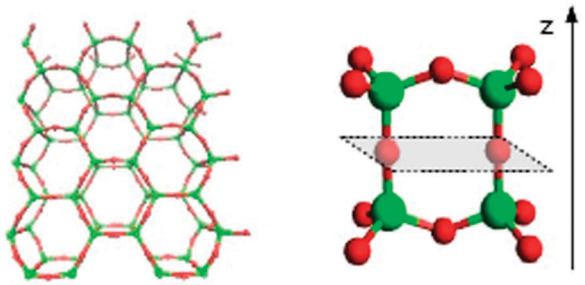

Fig. 1 (left: top view, right: side view) Two dimensional silica in its perfect crystalline state, according to ref. 3. Red = O, green = Si. The two layers are joined together along the tetrahedra height *via* common apical oxygens which define an indicated mirror plane.

atoms of the other component.[3] The full structure of this allotrope was proposed to be a bilayer structure with two tetrahedral units joined together with a common bridging oxygen in *Z* direction (Fig. 1, right). The nature of the bridging 'silicon–oxygen–silicon' bond is very interesting. From infrared reflection absorption (IRA) spectrum analysis together with DFT calculations, it was proposed that the angle is close to approx. 180 degrees in both the amorphous and the crystalline state.[12,13] This is very different from bulk amorphous silica where the Si–O–Si angles vary from 145–155 degrees. Therefore, a horizontal mirror plane and a vertical 3-fold symmetry axis was predicted to be present through these bridging oxygen atoms. As a consequence, in both the crystalline and the amorphous state, the top and bottom layer were predicted to have the same structure. The surface of the material was possible to study quite well using STM, which proves the two-dimensionality of the surface of silica bilayer (2D-silica in short).

Interestingly, the nature of the glass network structure had a very close agreement with the drawings of Zachariasen. The STM images showed that in the amorphous phase, 2D-silica is composed of a combination of several rings with various sizes. The crystal phase, on the other hand, was strictly made of 6 member rings. These six member rings were found to have some small disorder in the Si–O–Si bond angles,[3] similar to XRD and ND and *ab initio* studies. The ring distribution pattern for the amorphous phase was found to be lognormal which was qualitatively matched with Shackelford's tile model.[5] The binding energy of 2D-silica with the underlying Ru(0001)[9,13] or graphene surface[10] was found to be quite small. Hence, this ring distribution pattern on the surface should be an inherent effect of the amorphous phase of 2D-silica.

Recently, atomic rearrangements have been visualized by TEM in 2D-silica.[14] The authors were able to observe changes in the ring network structure under the impact of the imaging electron beam. A transformation from the 5-7-5-7 to the 6-6-6-6 ring was highlighted.

The ring distribution in amorphous graphene was also found to be similarly distributed as observed with recent Transmission electron microscopy (TEM) methods.[15] It was predicted that any two-dimensional network with trigonal geometry will have the same type of defect in its amorphous state, irrespective of the chemical nature of the structural units.[5,16]

1.2 Theoretical background: two-dimensional silica models

Previously, bulk-silica structure in three dimensions was simulated with Molecular Dynamics (MD)[17–19] and also with Monte Carlo (MC) methods.[20] The relaxation mechanism used for these MC simulations were based on the a bond-switching method, namely the Wooten–Winer–Weaire (WWW) algorithm.[21] Because of the similarity of ring distribution patterns of 2D-silica with graphene, ring networks of amorphous 2D-silica can be simulated with a 2D graphene-based model, just including one type of particles. MC and MD simulations were performed to understand properties of 2D-silica with such models. Kumar *et al.*[22] and Vink[23] had performed MC simulation with a graphene-based model with either a Tersoff-II potential[22] or a Keating potential.[22,23] An annealing process, coupled with bond-switching methods, was also performed with such models to generate a 2D ring network.[22] The ring distribution pattern and correlation measurements of such an annealed system did show close similarity with the available experimental data for 2D-silica.[24]

Wilson *et al.*[25] devised a method to generate the full 3D structure of 2D-silica, from an amorphous graphene template. They have shown that it is possible to minimise such reconstructed structure with a harmonic or TS potential while keeping the overall ring structure intact. Molecular dynamics simulations with a 3D force field were also used previously by Huang *et al.*[14] and recently by Zhang *et al.*[26] to equilibrate the 3D structure of 2D-silica. However, this applications required the detailed knowledge of experimental atom positions as a starting configuration and the MD simulations allowed for further local equilibration far below the glass transition. To the best of our knowledge, no classical 3D force field, based on previous 3D silica force fields, is available which allows one to simulate the 3 atomic layers in thermal equilibrium with a complete symmetry between the upper and lower layer.

Ab initio studies[9] were also employed to calculate the energies of several ring clusters of 2D-silica. For example, *via* DFT simulations the effect of strain[16,27] in hexagonal, haeckelite and other strained forms of 2D-silica could be analyzed. Recently, a DFT based analysis was performed on small cluster of amorphous 2D silica to understand the effect of different additives[28] such as aluminum, germanium, or potassium cations, embedded in 2D-silica.

1.3 Summary of the paper

In this work, we introduce a 2D model which on a semi-quantitative level is able to reproduce the different experimental observations of 2D-silica, including the spatial correlation of different ring sizes. Inspired by the success of the pair-wise BKS-potential to describe the properties of 3D-silica, we use a pair-wise potential for that modeling. Based on the excellent similarity between the observed IRA spectrum and the calculated harmonic IRA spectrum from a DFT optimised structure,[12,13] the symmetry between the two atomic layers were proposed. To incorporate this symmetry, we restrict the degrees of freedom of our model to two dimensions. A key issue for this comparison is the restriction to defect-free configurations which become rare for either high simulation temperatures and/or large system sizes. At the same

time a sufficiently large number of uncorrelated states need to be sampled in order to obtain good statistics.

The outline of the paper is as follows. In Section 2 we briefly repeat the required background for the experiments. Then, in Section 3, the simulation model is introduced. The generation of defect-free states is discussed in Section 4. In the subsequent Section 5 experiments and simulations are compared with respect to their structural properties such as pair correlation functions or angular distributions. Section 6 contains the results of the single ring statistics, whereas in Section 7 the spatial ring correlations, described in terms of doublets and triplets, are discussed. A study regarding spatial fluctuation of the rings are given in Section 8. We conclude with a discussion in Section 9. The scope of the article and possible future applications in the field physical chemistry is discussed in Section 10.

2 Relevant information about the previous experiments

Annealing of the experimental system was performed at 1180 K.[3] The resulting 2D-silica film turned out to have a mirror plane between the top and bottom layer. Thus, the observed structures can be characterized by a two-dimensional description. In this section, we summarize some crucial information which are relevant for either the model development or the procedure how to compare experiment and simulation in the present case.

The density of only the surface atoms (both silicons and oxygens) per unit area is relevant for 2D modelling. Since this is a classical model, we use the term particle instead of atom in the subsequent text. The surface particle density in the 2D plane can be directly calculated from the coordinates and is also available from the literature[29] (0.2068 surface-particles/Å^2). As the system is amorphous, the density varies locally in the 2D plane. The experimental coordinates are collected from ref. 3 as discussed above and used as the reference structure in our simulations.

The amorphous 2D-silica coordinates were obtained using STM methods separately for silicon and oxygen.[3] As it was not possible to sample silicon and oxygen coordinates at the same time, the authors devised empirical ways to generate them.[3,29] When observing the positions of the silicon atoms, the non-detected oxygen atoms were placed at the middle point of the line joining two closest silicon atoms. In the opposite case, the non-detected silicon atoms were placed at the center of a circumscribed circle encapsulating three nearest oxygen atoms. Although the ring statistics would be the same for both methods, some differences in the pair correlation functions and angle distributions in two dimensions are expected. The z-coordinates for silicon atoms were approximated *via* a DFT calculation.[3] Since we restrict the comparison to the 2D projection, these z-coordinates are of no relevance for the present work.

In both methods of generating 2D-silica coordinates discussed above, the resulting structural properties are very close to each other. Both methods generate very similar pair correlation functions, except for the first peak. Also, angular distributions for O–Si–O and Si–Si–Si angles are very similar in both cases (see ESI†). In this work we choose the coordinates, based on the direct observation of oxygen atoms. For this choice one also obtains a non-trivial distribution of the Si–O–Si bond angles which may be also compared with the simulations.

The experimentally reported configurations are defect-free, such that each silicon particle has three oxygen neighbors in 2D plane and each oxygen particle two silicon neighbors. We exclude the peripheral atoms from the statistical analysis because no information is available about their neighborhood. Since with the presence of dangling bonds the ring distribution is no longer well defined, only simulated defect-free configurations can be taken for comparison.

3 Simulation and modeling background

3.1 Approach towards a 2D model

In this paper, we want to study the ring statistics and dynamics at the surface of 2D-silica. For this purpose, we opted for a purely 2D model which represented the surface silicons and oxygens of 2D-silica. We wanted to study a model which automatically incorporates the observed symmetry between both layers, seen experimentally. Thus, structural and thermodynamic properties are fully characterized by 2D degrees of freedom. Naturally, only when studying the precise transformation between different ring sizes the 3D nature would be relevant.

As explained in Section 1.2, previous 3D modeling of 2D-silica involved equilibration of a 3D structure which was generated from a 2D model. However, there is yet no reliable force-field available for the 3D structure of 2D-silica. The 3D structure of amorphous 2D-silica was previously generated by Wilson *et al.*[22] from a graphene based model, *i.e.* the structure basically reflects properties of graphene. Also, a LAMPPS based modeling was performed by Huang *et al.*[14] and recently by Zhang *et al.*[26] However, these studies did not extend to generate transitions between any dynamical experiments. 2D bilayer ice, a structural analogue of 2D-silica, was previously simulated in 3D with molecular dynamics.[30,31] However, the dynamical simulations were only performed in a hypothetical confinement.

Also, the mysterious symmetry between the layers is not yet well understood. This particular symmetry requires the bridging oxygens to stay in a straight alignment with the two adjacent silicon atoms which is far away from the 'silicon–oxygen–silicon' angle (145 degrees) in standard 3D bulk silica. The previous 3D simulation approach, using a classical force-field, showed deviations from 180 degree in the bridging connections,[25] although the symmetry plane was present. However, a DFT optimized structure with fully 180 degree 'silicon–oxygen–silicon' angle in the bridging connection did predict excellent match with the observed IRA spectrum.[12,13] Therefore, using common silica force-fields like BKS in simulating 2D-silica is still questionable.

We have also neglected any quantum chemical calculations in this paper. Naturally, to obtain correct energies for a given structures, 3D-DFT is an option. However, it cannot be used to

generate a sufficiently large set of statistically uncorrelated structures (see later).

Since we are interested in ring statistics, one may argue about using a graphene based system with only one type of particles. Although graphene based models[22,24] do produce good correlation for the ring statistics, we do not want make such approximation at the beginning. Naturally, the presence of oxygens makes the model closer to the experimental system.

We chose to use MD methods to sample the equilibrium population of our model system. Previously, most of the theoretical simulations for investigating structure formation of graphene type systems involved a MC routine with a bond-switching algorithm. However, it is still unclear which kind of mechanisms are responsible for 2D-silica ring transformations and how they affect the equilibrium.[23] On the other hand, MD simulations do not restrict the system to a particular relaxtion path. Use of MD method have other benefits over MC, which will be discussed in the later sections.

For these reasons our analysis will be based on a binary 2D model with the goal to simulate the structure and thermodynamics of 2D-silica using molecular dynamics simulations.

3.2 Model potential

We have prepared a binary 2D model where two types of particles represent the surface silicon and oxygens. These particles are labeled as 'Si' and 'O', reflecting the types of the atoms in the top and bottom layer. Due to the symmetry between both layers, one may visualize the Si particles as '(top-layer silicon)–(bridging oxygen)–(bottom-layer silicon)'; and O particles as '(top-layer oxygen)–(bottom-layer oxygen)' units of 2D-silica (see Fig. 1).

The model force-field is prepared as a simple ionic model with charge ratio Si : O = (+1.5) : (−1) to guarantee charge neutrality. The Coulomb potential is approximated as a Yukawa potential. As shown by Méndez-Maldonado *et al.*[32,33] for Yukawa systems in two dimensions, it is possible to simulate ionic properties with that potential. We have used a softer core potential than Méndez-Maldonado *et al.* together with the Yukawa term. Thus, the inter-particle potential energy function (V_{ij}) can be written as,

$$V_{ij}(R_{ij}) = [(\sigma_{ij}/R_{ij})^{12} + (q_{ij}/R_{ij})\exp(-\kappa R_{ij})] \quad (1)$$

q_{ij} represents the charge ratio of the pair interactions with respect to Si–O interactions.

By construction this potential is dimensionless. In order to estimate appropriate values for the three parameters σ_{ij} we identify the unit distance with 1 Å. In what follows we will express all quantities except length in dimensionless units, *e.g.*, temperature as T^*, time as t^*.

The density of the system N/L^2 (N: number of particles, L: box length) is chosen such that it agrees with the experimental one (see above). Specifically, we require that the three nearest neighbor distances of the respective pair correlation functions, *i.e.* Si–Si, Si–O, and O–O, are matched (see further below). The resulting parameters are listed in Table 1.

The screening parameter κ is chosen as $2/L$, to resemble the long-range Coulomb potential as much as possible. We truncate and shift the potential and the corresponding forces such that the potential, as well as the derivative, are continuous at the cut-off. The cut-off distance (R_c) is given by $L/2$. The truncated and shifted potential function reads

$$V_{ij}^{\text{truncated}}(R_{ij}) = V_{ij}(R_{ij}) - V_{ij}(R_c) - V_{ij}'(R_c)(R_{ij} - R_c). \quad (2)$$

Table 1 Parameters of model potential

Interaction parameters	Si–Si	Si–O	O–O
σ_{ij}	2.250	1.075	0.900
q_{ij}	1.50	−1.00	0.67

3.3 Molecular dynamics simulations

The molecular dynamics simulations are performed with a software package, developed in our group. An important aspect of molecular dynamics is the system size. As discussed in Section 2 the analysis has to be based on defect-free configurations. For larger systems it turns out that the large majority of configurations is not defect-free for trivial statistical reasons. For this purpose we choose a relatively small binary system of 80 particles (32 Si particles + 48 O particles) with periodic boundary conditions (Fig. 2). In recent work we have shown that even for a 3D system a similar system size (N = 99) is sufficient to reproduce, *e.g.*, activation energies of oxygen and silicon diffusivity.[18] With the chosen system size it is possible to obtain a sufficiently large number of different defect-free states, which are taken as a basis for the comparison with the ESI,† key observables analysed in this work are basically identical for 80, 200, and 500 particles (except for a by far poorer statistics for large systems).

We choose a square box with side lengths of 19.67 Å and cut-off 9.8 Å. The cut-off distance was chosen such that all particles of two neighbor rings can interact with each other, ensuring that we take into account enough ring correlation effects. The ratio of these two types of particles are kept at 1 : 1.5 for Si : O to maintain the correct stoichiometry of 2D-silica in the 2D plane. The masses of the particles are chosen as 1 and 0.57 for Si and O, respectively. A constant volume–temperature (NVT) simulation is performed by coupling the box to a Nose–Hoover thermostat.[34]

The simulations are performed in equilibrium, *i.e.* the configurations are sampled from a Boltzmann distribution of

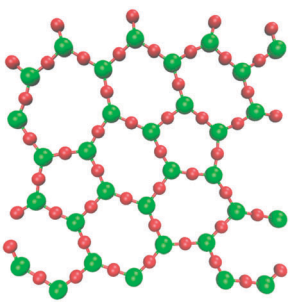

Fig. 2 A snapshot from the simulation at T^* = 0.015 with 80 particles.

the underlying distribution of states. The model system is simulated at 5 different temperatures ($0.014 \leq T^* \leq 0.016$) with a time-step ($t^*$) of 0.01. This specific temperature interval is motivated below. In all cases, the system is minimized at an interval of 100 steps to identify the underlying inherent states.[35] This minimization procedure, taking out the vibrational energy, has several advantages. First, this allows a closer comparison with the frozen-in experimental configuration. Second, this procedure is the basis for the determination of the underlying density of states *via* Boltzmann re-weighting, as outlined below. Third, a clear-cut identification of defect-free states becomes possible. After this analysis step the simulation is continued with the previous configuration and momenta. A total of $\sim 2.5 \times 10^5$ steps are recorded for each temperature.

Whereas the length scale can be extracted from the comparison with the experiment, this is not possible for the energy scale since the experiments are performed for relatively lower temperatures where no ring rearrangement can be observed. Temperatures above 1300 K are not accessible experimentally because the silica layer detaches from the substrate. As discussed in the ESI,† comparison with previous DFT calculations in ref. 3 yields an energy scale of 57 eV; which, however, should be taken as an upper limit. As a consequence, the simulation temperature 0.015 corresponds to approx. 9700 K (again upper limit). Furthermore, we discuss that the choice of our simulation temperatures does nevertheless allow us to extract structural information, relevant at much lower temperatures. The physical implication of this high temperature is discussed further below.

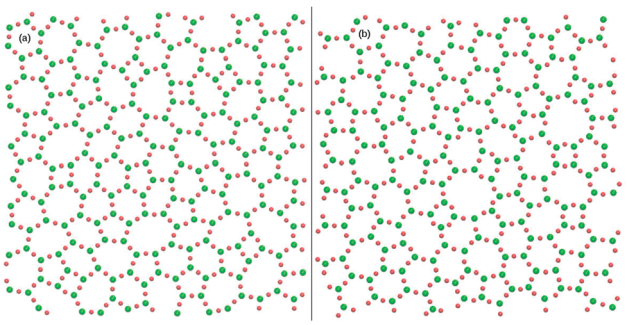

Fig. 3 (a) A snapshot from the simulation at $T^* = 0.015$ with 500 particles. (b) Experimental structure collected from ref. 3, with the experimental method described in the Section 2. Note the apparent similarity. It will be shown that the 500 particle simulation agrees very well with the 80 particle simulation (see ESI†) and that the latter agrees in great detail with the experimental structural results.

4 Generation of defect-free states

4.1 Identification of defect-free states

In order to filter out the minimized configurations with defects for the subsequent analysis, we use a fixed Si–O bond distance cut-off of 2.0 and Si–Si bond distance at 3.6. We check that each type of particles are defect-free, *i.e.*, they have the required number of neighbors for silicon–oxygen, oxygen–silicon and silicon–silicon combinations. The choice of that bond distance cut-off is based on the observation that the first neighbor peak in the silicon–oxygen and silicon–silicon pair correlation function has basically decayed to zero for that distance. All states which contains at least one particle with defect, is considered as a defect state. Ring edges are defined by Si particles which share a common O particle. In Fig. 3 we show an experimental configuration together with one of the very few defect-free simulated systems with 500 particles. On first sight both configurations look very similar. This will be quantified for different relevant observables (taking the 80 particle rather than the 500 particle system).

Since the efficient generation of defect-free states is of major relevance, we start by showing the energy distribution $P_{IS}(E_{IS})$ of inherent states in Fig. 4, distinguishing states with and without defects and sampled for different temperatures ($0.014 \leq T^* \leq 0.016$). The energy distribution shows two distinct peaks, corresponding to defect-free and defect states. Typically, the presence of defects gives rise to higher energies. Since the defect-free states have lower energies, their Boltzmann probability decreases with increasing temperature; see Table 2. From Fig. 4 it is clear that all simulated configurations at low energies are defect-free.

Most remarkably, the lowest energy, encountered during the simulations, does not change upon variation of the temperature. This directly shows that in analogy to 3D BKS silica there exists a low-energy cutoff[18] in the potential energy landscape of the

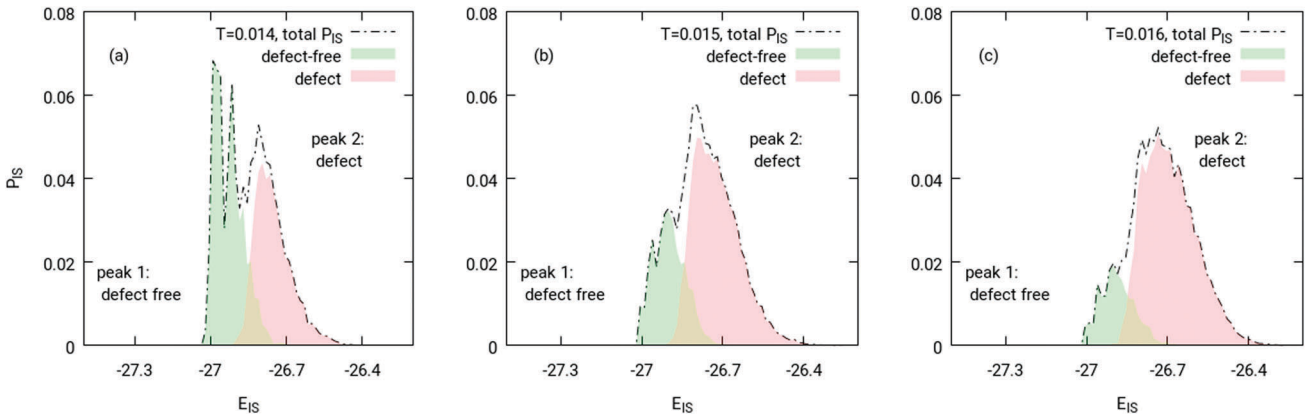

Fig. 4 Inherent states probability distribution at $T^* = 0.014$, 0.015, 0.016. Shaded areas shows population of defect-free (green) and defect (red) states.

Table 2 Fraction of defect free states, the statistical efficiency (see main text) and the variance of the ring-size distribution at different temperatures

Temperature	Fraction of defect free states	Statistical efficiency	Variance of ring-size distribution
0.014	0.54	0.0010	0.97
0.0145	0.45	0.0010	0.98
0.015	0.31	0.0015	1.06
0.0155	0.21	0.0016	1.08
0.016	0.18	0.0019	1.11

disordered states. Such a cutoff is not observed for, *e.g.*, Lennard-Jones type systems and results as a consequence of the network structure.[18]

As a consequence, in the chosen temperature regime the observed inherent structures of defect-free states are identical to those which would be sampled during a simulation at much lower temperatures where, let's say, 99% of all configurations were defect-free. We conclude that the high temperature, used for reasons of statistical efficiency, yields results which enable a direct comparison with the low-temperature experimental results. We remind that the same property was also explored for the simulations of 3D BKS silica.[18]

4.2 Correlation times

For amorphous systems the relaxation times can strongly increase when decreasing the temperature. Thus, the overall statistical efficiency requires the knowledge of the fraction of defect-free states relative to the inverse time until the configuration is uncorrelated, *i.e.*, τ_r. The latter can be extracted from the ring auto-correlation function

$$\Delta_r(t_0,t_0+\delta_t) = \langle\langle(1-\delta_r)\rangle\rangle \quad (3)$$

Here, $\delta_r = 0$ or 1 depending on whether a particular ring, which is defined by the indices of its corners, still exist after a time-lag δ_t or not. This time-lag is actually the frame gap in between the defect free states. For each ring-size, this quantity is averaged over all rings of size 'r' in all frames with time-lag δ_t. This quantity has a maximum value of 1 and vanishes for long times; see Fig. 5(a) for the different decay functions. For each curve we extract the average correlation times τ_r from the area of the curves of the decay function, respectively. The results are shown in Fig. 5(b) as a function of temperature and ring size. As expected the ring size 6 is by far the most stable one.

The results are also included in Table 2. In turns out that the statistical efficiency is highest for $T^* = 0.016$. A temperature decrease to $T^* = 0.015$ only displays a weak reduction in the statistical efficiency, whereas a larger reduction is found for a further decrease to $T^* = 0.014$.

It also turns out that within the sub-ensemble of defect-free states the 'diversity' of states is higher for higher temperatures as reflected by the temperature-dependent variance of the ring-size distribution, also given in Table 2. This is a natural consequence of the fact that amorphous structures with many six-rings are energetically favorable and are mainly observed at low temperatures. Note that the observed variance at a temperature of 0.015 is close to the experimental value (2D-silica ring-variance = 1.06).[36] Therefore, we will restrict ourselves to that temperature in the subsequent analysis.

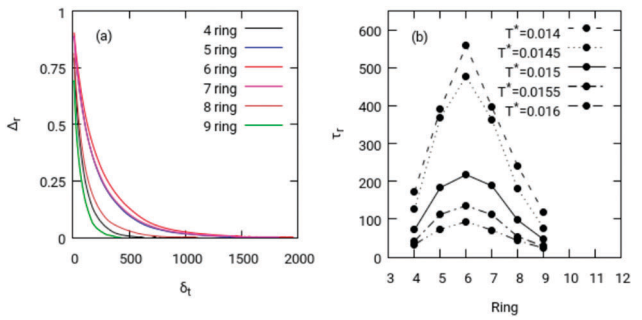

Fig. 5 (a) Decay of ring auto-correlation function (Δ_r), for individual rings, at $T^* = 0.015$. (b) Average relaxation time (τ_r) as a function of ring size and temperature.

5 Structure: comparison between experiment and simulation

5.1 Pair correlation functions

The experimental and the simulated pair correlations functions are shown in Fig. 6. By construction the distances of the three

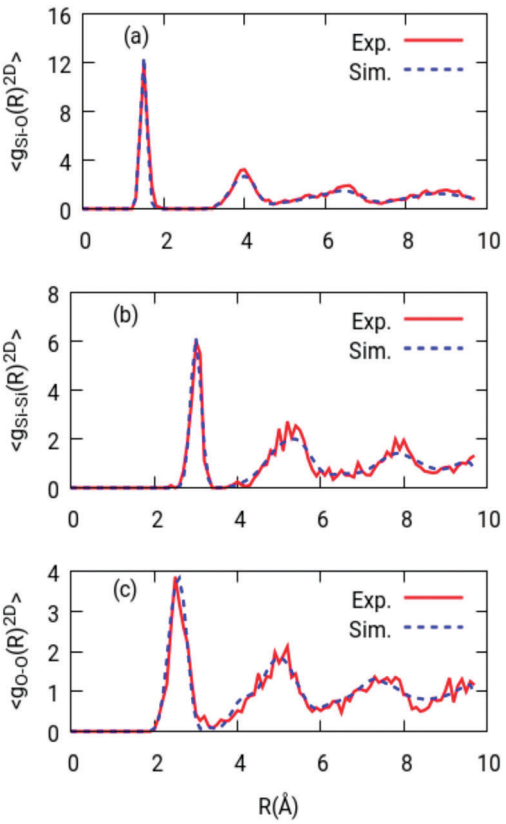

Fig. 6 The experimental and simulated pair correlation functions for (a) Si–O pairs, (b) Si–Si pairs, (c) O–O pairs. The experimental reference structures are provided in ref. 3. Simulations data are convoluted with a Gaussian function of width 0.12 Å for Si–Si and 0.08 Å for Si–O and O–O, respectively. Only defect-free states are taken for the analysis.

nearest-neighbor peaks agree very well between experiment and simulation (Si–O: 1.5 Å, Si–Si: 3.0 Å, O–O: 2.5 Å). Remarkably, also the positions and widths of all the other peaks agree extremely well for all three pairs. This agreement suggests that this simple model allows one to reproduce the structure in great detail.

Initially we found a sharp $g(r)$ for the nearest neighbor peaks for Si–O and Si–Si. The sharpness is indeed not very different from previous BKS-simulated defect-free vitreous bulk-silica structures.[20] In order to obtain the agreement of the experimental and simulated width of the nearest neighbor peaks it was necessary to convolute the simulated pair correlation functions by a Gaussian with widths 0.12 Å for Si–Si and 0.08 Å for Si–O and O–O, respectively. This convolution is supposed to reflect the finite resolution in the experiments. The unconvoluted data can be found in the ESI.†

5.2 Angular distribution

The angle distributions from all defect-free states are collected and compared with the experimental structure (Fig. 7 and Table 3). The angle distributions are calculated for the corresponding set of atoms which lie within a chosen bond-length from each other. The angle distribution of Si–Si–Si and O–Si–O of the model show an excellent matching with the average angle distribution pattern of 2D-silica. The Si–O–Si angle distribution is too narrow as compared to the experimental data. One might use additional three-body potentials to optimize the agreement between simulation and experiment. However, because we are mainly interested in the network structure, as defined by the Si particles, we refrained from this additional complexity.

5.3 Inner ring angles

Here we show the distribution of the inner ring angles as a function of ring sizes (see Fig. 8(a)). Trivially, the average inner ring angles are fixed by the geometric properties of a ring. Whereas small rings display relatively small deviations around their average angle, these deviations strongly increase for larger rings. In Fig. 8(b) these fluctuations are compared with the experimentally observed fluctuations. The agreement is again very promising, except for deviations for the largest two ring sizes (8 and 9-ring). In any event, since large 9-rings are quite rare in the experiment, we may state that the current version of the force field can closely reproduce the angle distributions for the most frequently occurring rings in agreement with the results in Fig. 7(c).

Table 3 Mean angles in Fig. 7

	O–Si–O	Si–O–Si	Si–Si–Si
Experiment	120.1	164.7	120.0
Simulation	119.6	175.9	119.7

6 Single ring statistics

6.1 Ring size distribution

The distribution of ring sizes is plotted in Fig. 9. The average value of the ring sizes for the experiment is 5.981, whereas for the simulation it is strictly 6 because of periodic boundary conditions. We find a reasonable agreement between experiment and simulation. The main deviation in relative terms is observed for ring size 7.

6.2 Correlation analysis for the experimental data

For a quantitative comparison between simulation and experimental data it is essential to determine the statistical errors. This is a non-trivial task because, on the one hand, ring sizes of spatially adjacent rings are expected to be correlated and, on the other hand, subsequent simulated configurations are strongly correlated as well.

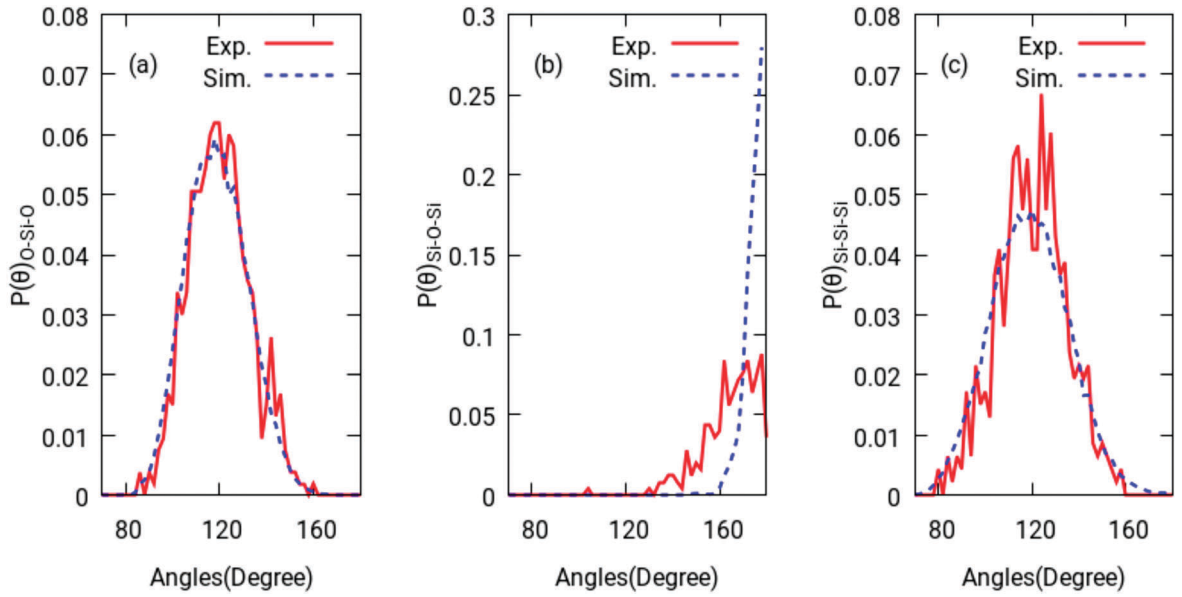

Fig. 7 Angle distribution comparison between real 2D silica and our model system for (a) O–Si–O, (b) Si–O–Si, and (c) Si–Si–Si. In (a) and (b), the Si–O cutoff is chosen as 2.0 and in (c) the Si–Si cutoff as 3.6.

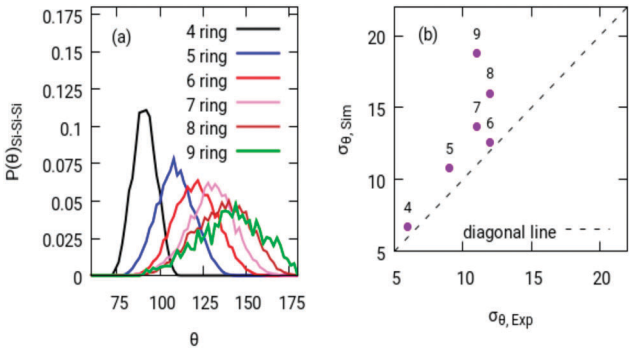

Fig. 8 (a) Inner Si–Si–Si angle distribution for various ring sizes from simulation data. Each data set for ring sizes are self-normalized. (b) Comparison between experimental and simulation data for the standard deviation (σ_θ) for different ring sizes. The experimental values were collected from ref. 29.

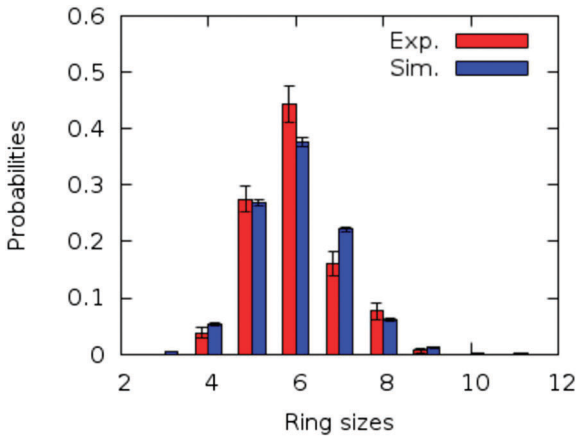

Fig. 9 Comparison of the experimental and numerical ring size distribution. The experimental data are taken from ref. 37. For the numerical data we only take into account the defect-free states.

For the experimental data with a total of 317 rings, the estimation of the statistical uncertainties are carried out by performing a block analysis. For this purpose we divide the coordinates into $M = 9$ boxes with approximately 35 rings per box (see Fig. 11). Only rings with no open edge were taken into account. Detailed data is given in the ESI.†

The error bars in Fig. 9 are the standard errors of the estimated ring-size probabilities (P_r^m) from each set, i.e,

$$\mathrm{SE}_r = \sqrt{\frac{1}{M(M-1)}\sum_m \left(P_r^m - P_r\right)^2} \qquad (4)$$

This actual standard error can be compared with the case that the occurrence of an r-ring is independent of the number of r-rings in the neighborhood. In this extreme limit the distribution is binomial and reads

$$\mathrm{SE}_r^{\mathrm{bpd}} = \sqrt{P_r(1-P)_r/NM}. \qquad (5)$$

Here, N is the number of rings per configuration. Now, a comparison between SE_r and $\mathrm{SE}_r^{\mathrm{bpd}}$ allows one to estimate

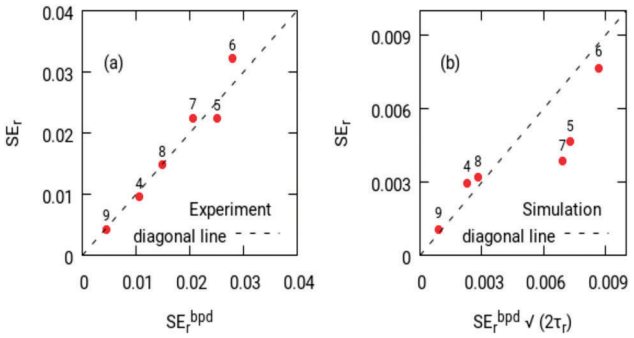

Fig. 10 The statistical error SE_r is shown along the ordinate for (a) experimental data and (b) simulation data. The abscissa displays the hypothetical statistical error if all configurations were statistically independent and no spatial correlation of r-rings with themselves are present.

correlations among the ring sizes of the adjacent rings. As shown in Fig. 10(a), correlation effects are only significant for $r = 6$, reflecting a favourable grouping of 6-rings. For all other ring sizes these self-correlations are very small, if at all present. Of course, this does not imply that correlations among different ring sizes are small. For example it will turn out that a 5-ring attracts 8-rings in its neighborhood.

6.3 Correlation analysis for the simulated data

For the calculation of the statistical error for the simulated data, we again perform a block analysis and divide the total trajectory of defect-free configurations into $M = 34$ sets with $N = 2500$ subsequent configurations. As each frame of the system contains 16 rings, the total count of rings was $\sim(85000 \times 16)$. In analogy to the experimental data this allows us to calculate the statistical uncertainty SE_r; see Fig. 10(b).

Due to the strong correlation of subsequent configurations this estimate is much larger than estimated from the binomial distribution. The difference is reflected by the correlation times τ_r, already shown in Fig. 5(b). Multiplying $\mathrm{SE}_r^{\mathrm{bpd}}$ with $\sqrt{2\tau_r}$ (for $\tau_r \gg 1$) allows one to estimate the true statistical uncertainty.[38] Indeed, as shown in Fig. 10(b) these values agree reasonably well with the actual statistical uncertainties, resulting form the block analysis. We have no direct explanation for the remaining deviations for $r = 5$ and $r = 7$.

Collecting all information together, it is possible to draw the error bars in Fig. 9. These error bars are sufficiently small so that the remaining differences between experiment and simulation are real.

7 Spatial ring correlations

7.1 General

The previous analysis was sensitive to the question whether an r-ring likes or dislikes to have another r-ring in its neighborhood. Here, we generalize this question and analyze the occurrence of doublets and triplets. doublets are defined as two rings sharing a common edge and triplets as three rings, sharing a common corner.[37] This is sketched in Fig. 12.

To compare with the experimental distribution, we filter all defect-free states and determine all doublets and triplets, containing

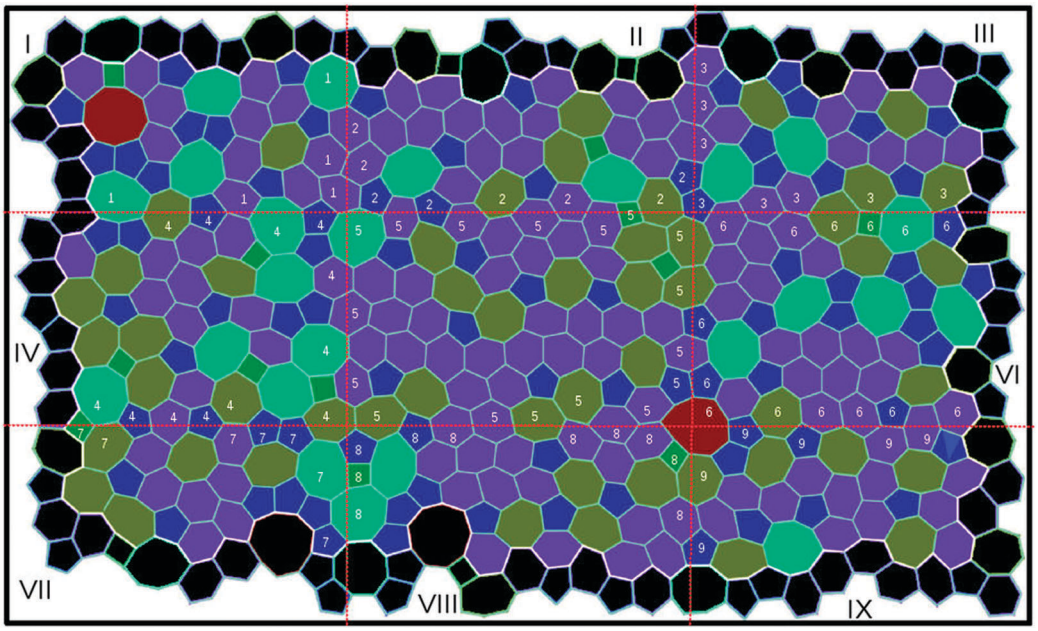

Fig. 11 Structure collected from ref. 37 and reproduced with permission from *J. Non-Cryst. Solids* Copyright 2016 Elsevier B.V. The structure was divided in 9 equal blocks. The black rings were excluded from ring counting. The overlapping rings were assigned to the respective blocks depending on the area covered by the rings inside each overlapping block. Assigned block numbers were mentioned inside such rings.

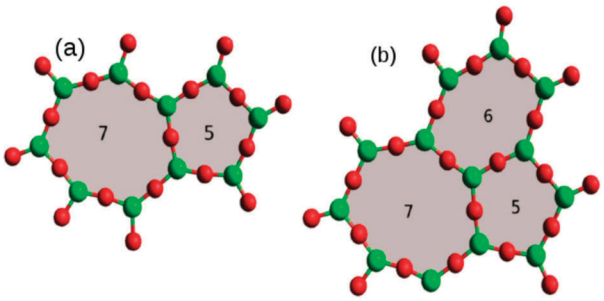

Fig. 12 Example of (a) a doublet, sharing a common edge, and (b) a triplet, sharing a common corner.

rings with ring-sizes between 4 and 9. For a reliable comparison with the experimental data, we only take into account combinations with probability of more than 1%. For this lower limit the estimated error for the experimental data is approximately one third of the value itself as estimated from the binomial statistical error.

In the simplified case of uncorrelated spatial arrangement of rings, one can simply reproduce the probabilities of these ring combinations by multiplying individual ring probabilities with an appropriate permutation factor. In this case the predicted probabilities are given by

$$P_{ijk\ldots}^{\text{predicted}} = pf \cdot \prod_i P_i \tag{6}$$

The permutation factor pf is given by

$$\begin{aligned} pf &= 1, \quad \text{for } i = j \\ &= 2, \quad \text{for } i \neq j \end{aligned} \tag{7}$$

for a doublet and

$$\begin{aligned} pf &= 1, \quad \text{for } i = j = k \\ &= 3, \quad \text{for } i = j \neq k \\ &= 6, \quad \text{for } i \neq j \neq k \end{aligned} \tag{8}$$

for a triplet.

This permutation factor counts, in how many ways a given combination of rings can be generated. Thus, in this uncorrelated scenario, the value

$$P_{ijk\ldots}^{\text{eff}} = \frac{P_{ijk\ldots}}{P_{ijk\ldots}^{\text{predicted}}} \tag{9}$$

is constant. As a consequence this 'effective probability' reflects the degree of compatibility of the rings, forming a doublet or a triplet, respectively. An additional advantage of the effective probabilities as compared to the bare probabilities becomes relevant when comparing experiment and simulation. As discussed in the context of Fig. 9 the ring statistics is slightly different. However, when comparing the effective probabilities this difference is taken out and one can directly compare the amount of spatial correlations. For all subsequent experiment–simulation comparison graphs, we have taken the experimental values from ref. 37.

7.2 Properties of doublets

In Fig. 13 the experimental and simulated doublet probabilities are compared. The data agree very well. Note that the absolute values of the probabilities vary by two orders of magnitude.

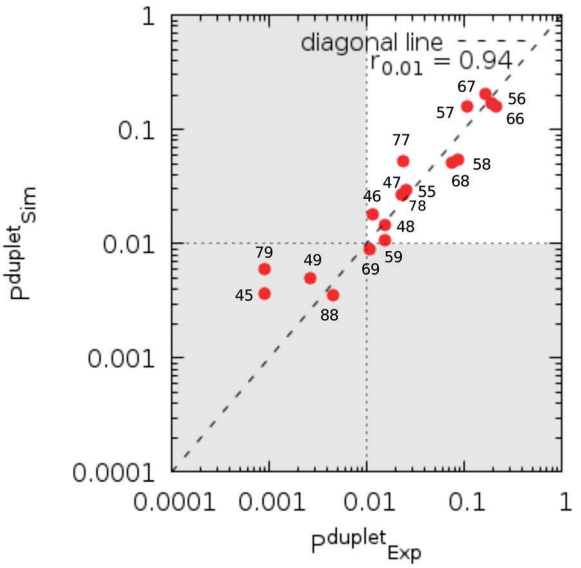

Fig. 13 Comparison of the probabilities of all doublets found by both experiment and simulation. The shaded area reflects probabilities <1%.

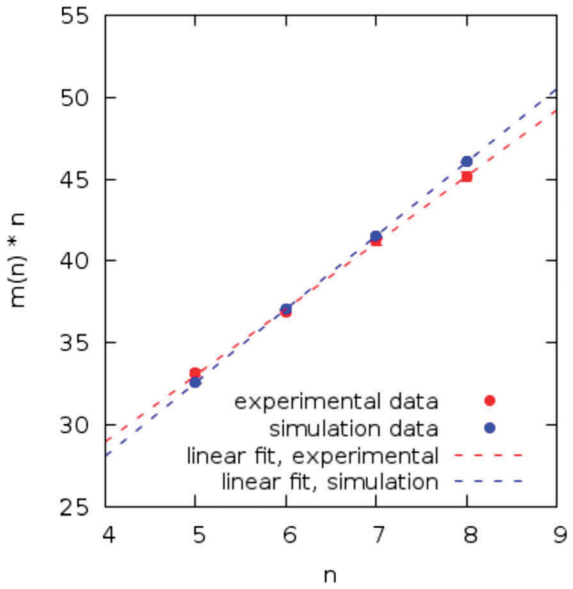

Fig. 14 Comparison of experimental and simulation data with Aboav's theory for ring-sizes 5–8. The data is fitted linearly in both cases. For the experimental (numerical) one obtains a = 1.95 (a = 1.51) with an intercept = 12.6343 (10.1217).

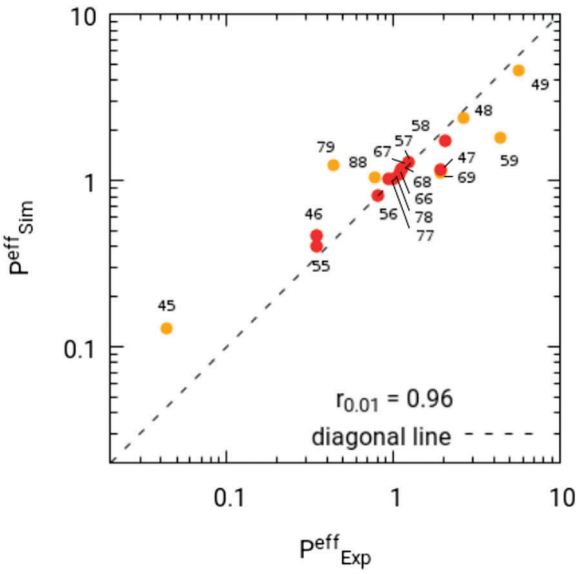

Fig. 15 Comparison of effective doublet probabilities. All doublets which have $P_{ij}^{predicted} > 0.01$ as well as $P_{ij} > 0.01$ for both experiment and simulation are marked in red. The correlation coefficient is calculated for the red points only.

The fluctuations in the lower part of Fig. 13 also reflect the large statistical uncertainties of these low-probability doublets.

Properties of the neighborhood of a ring in a triangular network were previously analyzed by Aboav[39] and later by Weaire *et al.*[40] and Rivier *et al.*[41] In case of an ideal situation, a ring of a certain size (n) should have no preference towards its nearest neighbor ring, which share a common edge. Therefore, the average neighbor ring size ($m(n)$) of any ring should be equal irrespective of its size. However, this average changes when certain rings prefer rings of certain size in their neighborhood. In general, for macrosystems like cells and soaps, it was observed that $m(n)$ is inversely proportional to n.[40] A generalized theory was proposed to calculate the average ring size of the neighborhood of a ring as

$$m(n) = 6 - a + \frac{6a + \mu_2}{n} \quad (10)$$

Here, m is the average ring-size of the neighbors of ring-size n. The factor 'a' measures the overall effect of correlations in between the rings. As shown in Fig. 14, both data-sets are reasonably matched for ring-sizes 5–8, which are most common in the system.

As suggested by Weaire *et al.*,[40] the case $a > 1$ generally suggests a tendency to minimize strain of a ring by having appropriate neighbors, *i.e.* introducing spatial correlations of specific ring sizes. In case of trigonal atomistic networks like 2D-silica, this strain usually occurs due to angle distortions at the corners. As discussed above, the spatial correlations are best analyzed by studying the effective probabilities P_{ij}^{eff}. As shown in Fig. 15, P_{ij}^{eff} varies by more than an order of magnitude, reflecting the importance of spatial correlations. We observe a very high correlation coefficient 0.96. This result is maybe the most sensitive test concerning the very good agreement between simulation and experiment.

Doublets with large values of P_{ij}^{eff} contain one large ring ($r > 6$) and one small ring ($r < 6$) component (*e.g.* '58'). In contrary, particularly small effective probabilities occur for a combination of two small rings (*e.g.* '55'). This suggests that the coupling between large and small rings through edges give rise to the extra stabilization. This effect can be directly seen in Fig. 16 where the effective probabilities for doublets are shown in a different representation. For small rings, the effective probabilities increase with increasing ring size of the second ring. For large rings the opposite holds true.

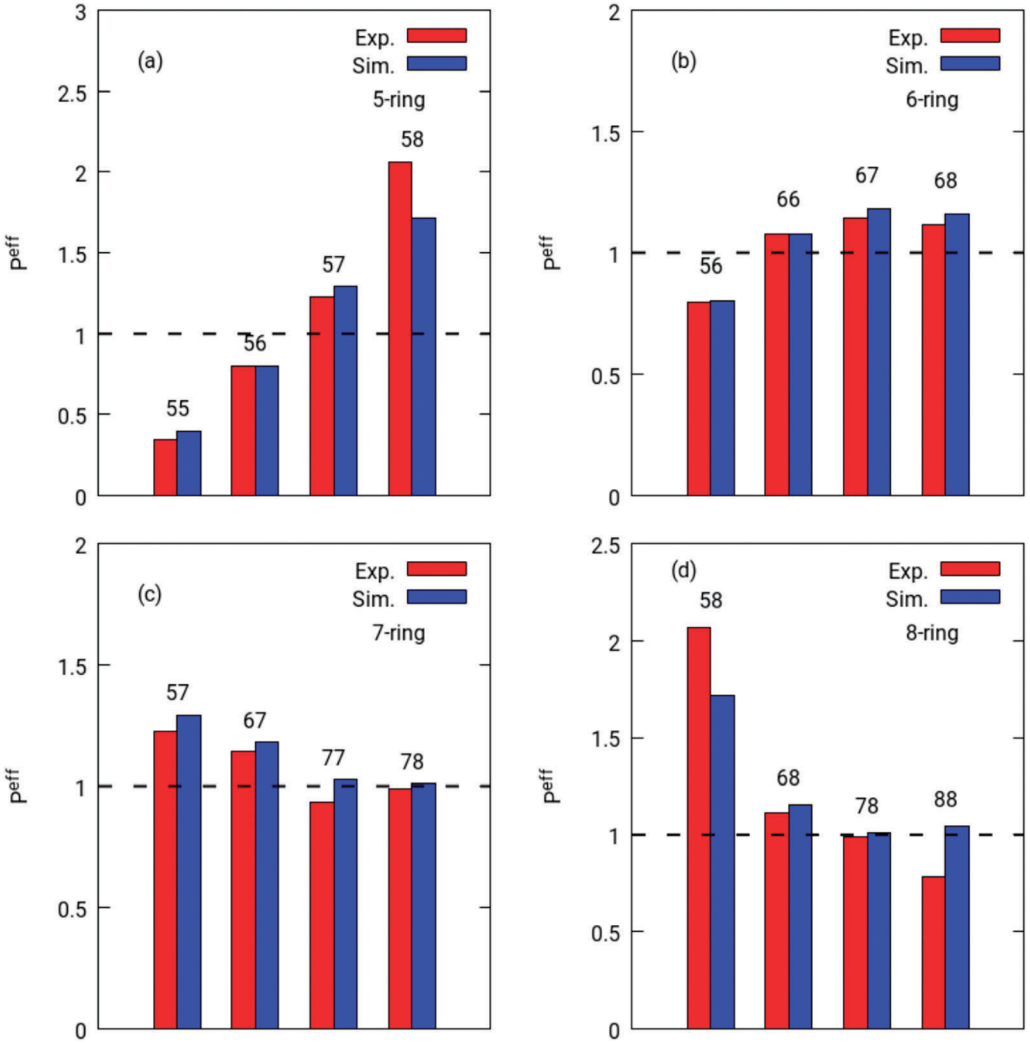

Fig. 16 P_{ij}^{eff} values sorted with respect to ring sizes of (a) 5, (b) 6, (c) 7, (d) 8. The dashed line marks $P_{ij}^{\text{eff}} = 1$, reflecting the limit of vanishing spatial correlations.

7.3 Properties of triplets

In analogy to the case of doublets, the same statistical analysis can be performed for triplets. One expects that the triplets show a different correlation effect than the edge sharing doublets. As discussed by Büchner *et al.*,[37] these corner sharing triplets can be considered as the building blocks of the triangular network. As all three rings join at a single corner the total angle has to be 360 degrees. This condition gives rise to selectivity effects.

The probabilities of the individual triplets show good agreement with the experimental data (Fig. 17). The most probable triplet was 567, predicted both by simulation and experiment.

Also the effective probabilities of triplets match very well between experimental and simulated data (Fig. 18). In analogy to the case of doublets, the triplets with large–small ring combinations also shows higher values of effective probabilities as compared to small–small ring combinations.

Theoretically, a large ring has higher chances to deform because of its size and flexibility whereas the smaller rings should have a stricter geometry. Thus the strain caused by a neighbored small ring does not build up if a large ring is present nearby. Also, to keep the total angle around each corner at 360 degrees, a large ring is necessary in a triplet if one of the rings is small. This effect may, *e.g.*, explain the relation $P_{\text{eff}}(567) \approx 2P_{\text{eff}}(566)$, observed numerically as well as experimentally.

8 Spatial fluctuations of rings

In Section 4.2, we have determined the average life-time of each ring. In this section, we investigate how the spatial co-ordinates of the corners in the ring fluctuate during its life-time. These fluctuations can be directly related to the thermally broadened intensity in scattering experiments.[42,43] Of course, experimentally one can only see the average effect from all rings. The present simulations allow us to see the fluctuation behavior of the individual ring sizes.

To analyze the fluctuations during the life-time of a specific ring we naturally have to choose the real trajectories in this calculation. We monitor the co-ordinates of each ring-corners

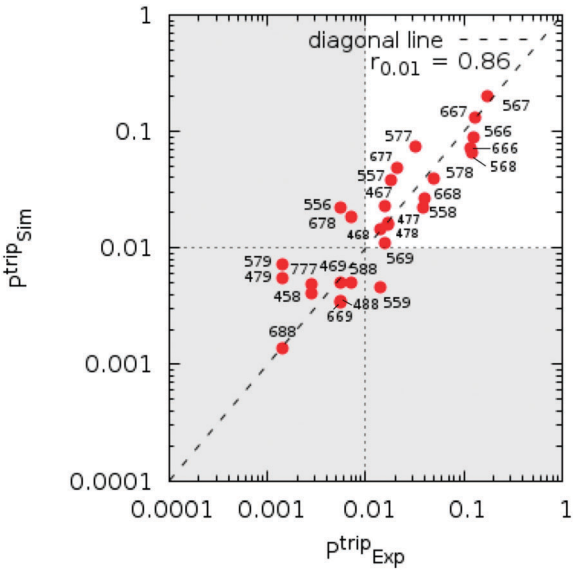

Fig. 17 Comparison between simulation and experimental triplet data for all triplets found by both experiment and simulation. The shaded area reflects probabilities <1%.

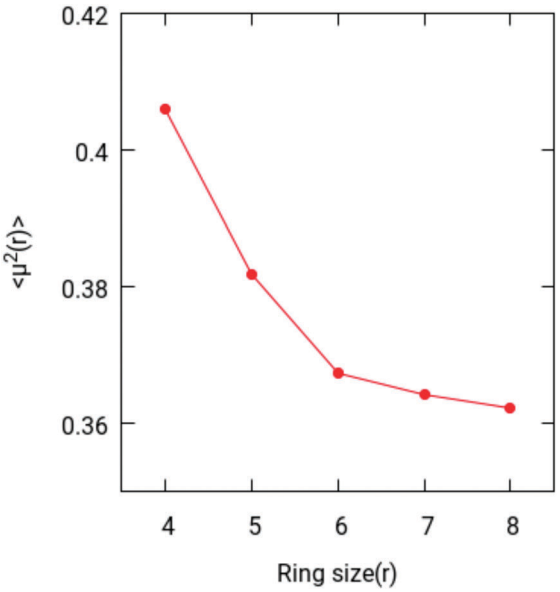

Fig. 19 Average variance of spatial fluctuation for each ring up to 50 sampled steps.

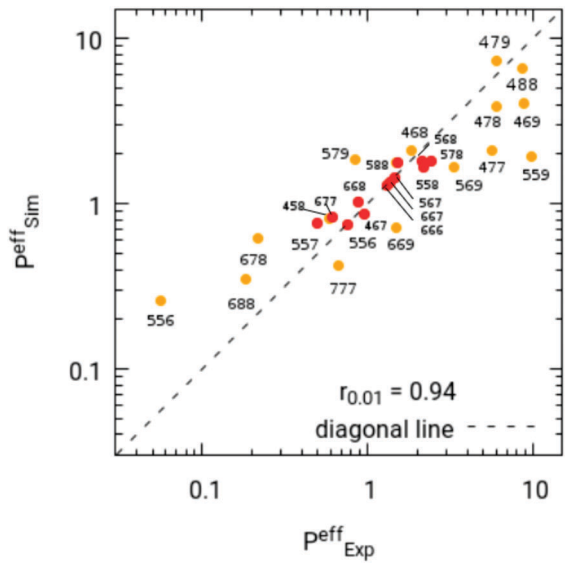

Fig. 18 The comparison of effective triplet probabilities. All triplets which have $P_{ij}^{predicted} > 0.01$ as well as $P_{ijk} > 0.01$ for both experiment and simulation data are marked in red. The correlation coefficient is calculated for the red points only.

(Si particles) from the real trajectory, as long as the corresponding ring appear in the minimized trajectory. From these data we directly obtain the variance of the X and Y coordinates $(\mu_i^2(X),\mu_i^2(Y))$ for each Si particle. The total variance is taken as $\mu_i^2 = \mu_i^2(X) + \mu_i^2(Y)$. For a ring of size r this variance is averaged over all r Si atoms of that ring. Then this analysis is repeated for all rings of size r.

Clearly, the variance will increase with the number of acquired data. Naturally, the variance will be higher for 5, 6 and 7 rings since they have larger life time. Therefore, we cannot obtain information about the immediate fluctuation of the rings from the full trajectory analysis. To overcome this problem, we chose a limiting time for all rings to calculate $\langle\mu^2(r)\rangle$. The limiting time is chosen as $\tau_9 \sim 50$ steps, such that we obtain sufficient data for small and large rings. The averaging procedure of $\langle\mu^2(r)\rangle$ is performed for the 50 initial steps for all rings of ring-size r, which live for at least 50 steps.

The results are shown in Fig. 19. The variation of the fluctuations as a function of ring size is quite small (10%). Looking in more detail we find that the small rings show a slightly larger variance, while for larger rings the variance is nearly constant. A possible explanation is the diffusion of the center of mass during the chosen time. Small rings with only a few atoms are expected to show larger diffusion. This will slightly bias the average $\langle\mu^2(r)\rangle$ calculation.

9 Conclusions

Using a Yukawa-type force field we have succeeded in reproducing key structural features of the experimentally studied silica film. Assuming an identical top and bottom layer, as suggested by the experimental observations, we can effectively use a purely 2D model. As shown in this work, the structural properties and in particular the ring statistics can be reproduced very well. A conceptual key aspect is the preparation of defect-free states in equilibrium which requires low but not too low temperatures. In particular, this constraint requires the use of relatively small systems. With the help of MD simulation, we are able to sample the equilibrium distributions for both defective and defect-free states. Although the defect states do not have any effect on the ring distribution, they do occupy a significant portion of the energy landscape (Fig. 4). From previous studies, we know that coordination defects in bulk-silica play an important role in glass formation.[18]

It will be interesting to perform similar study for 2D-silica with the sampled defect states.

We have found that despite the small deviations in the ring statistics, the doublet and triplet statistics and the effective ring probability plot showed very good correlations with the 2D-silica system. In general, it is essential to use the effective probabilities for a fair comparison because the residual differences of the ring statistics are, at least to a large extent, removed. The main remaining differences are related to the oxygen positions which are too close to the connection line between two silicon atoms.

Conceptually, it was essential to use relatively small system sizes. Studying possible finite size effects is difficult since the availability of defect free states exponentially decreases with increasing system size. Nevertheless, by using extensive simulations to obtain a few defect-free configurations we have checked that for the statistical observables, analyzed in this work, finite size effects are small. Furthermore, it may be interesting to perform full 3D simulations of the system in order to reproduce the conditions under which the top and bottom layer of the system are basically mirror images of each other, as observed experimentally. This would involve the development of an appropriate 3D force field, reflecting the energies as obtained by the corresponding DFT-calculations.

As derived from the analogy to 3D silica and as discussed above, the properties of the subensemble of defect-free configurations corresponds to the properties of states, generated at much lower temperatures. Thus, the properties of the experimental system, corresponding to a low-energy configuration (as reflected by the absence of defects), can be directly compared to the results of simulations at somewhat higher temperatures.

Interestingly, the required temperature scale (with an upper bound of approx. 10 000 K) for the 2D system to achieve sufficiently fast equilibration is much higher than the corresponding simulation temperatures of 3D silica (lower than 3000 K). This may be related to the fact that typical barriers in 3D are lower due to the higher number of degrees of freedom. Furthermore, it is conceivable that in the present system the barrier might be smaller (and, thus, the accessible temperature range lower) if during the transitions between different inherent states one would allow for a local suspension of the symmetry between both layers. In any event, this is beyond the 2D model, promoted in this work.

10 Outlook

This work mainly serves the purpose to show that the 2D model is able to reproduce many experimental observations in great detail. Also additional information, only accessible from computer simulations, was presented. For example additional insight about the life-times and the spatial fluctuations of the different ring sizes can be analyzed. In general, the verification of the 2D model will allow us to explore a large variety of additional information, not accessible experimentally. For example, one may study the potential energy landscape of the total 2D system. In this way, a detailed comparison may be possible with standard bulk silica where an extensive analysis of the potential energy landscape was previously performed.[18] One important aspect of the simulation is a clear identification of defect- and defect-free states and how their probabilities change with temperature. This information is not possible to obtain in experiment, since the required temperature would be too high. In Fig. 4, the presence of a cut-off energy in both defect and defect-free states can be identified. This observation may be explored in future work in the framework of the potential energy landscape in order to elucidate the properties of the glass formation and the Kauzmann paradox.

The 2D model has also great potential for application in the field of 2D continuous random networks (CRN). One may study the impact of local ring energies on the formation of local doublet or triplet structures. Since our model is strictly 2D, we cannot directly compare dynamical properties (*e.g.* mechanisms) with the real system. However, this model is an excellent example of a 2D network-glass where a clear identification of the rings is possible. Studying various relaxation paths of the network structures through molecular dynamics, one may hope to obtain a better mechanistic understanding of the resulting structures. This might in turn help to develop a more general Monte-Carlo algorithm for sampling various CRN in equilibrium in analogy to ref. 23.

The Yukawa-type model also has potential application in the development of various computational tools. As we have discussed before, the previous 3D DFT calculations of 2D-silica were primarily based on a graphene based CRN. As the structure of the current Yukawa model agrees extremely well with the experimental observations, it may be considered as a better starting point than the structure of graphene.

There are various other 2D materials where the present Yukawa-type model can be applied; see Fig. 20. It is important to remember that the force-field does not incorporate any substrate interaction. One may need an additional angle-dependent force field for simulating binary mono-layer materials such as nitrogenated graphene (C_3N) or hexagonal boron nitride (hBN). Another prime candidate for application of this model is two-dimensional ice. It was possible to grow an ice mono-layer[44] to a bi-layer and a multi-layer[45] on a Ru or a Cu surface. Theoretically, the bi-layer ice was previously simulated with molecular dynamics within confinement.[30,31,46] It shows almost similar ring distribution and structure compared to 2D-silica.

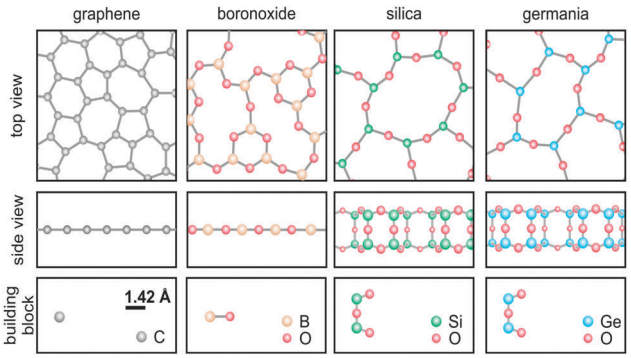

Fig. 20 Various analogue of 2D-silica type materials in two dimensions. The drawings are inspired from ref. 3, 47, 48 and 49, respectively.

However, the layer symmetry of bi-layer ice is not as good as in 2D-silica.

The study of two-dimensional materials is an active field of research with various examples coming to light every year. From monolayer graphene to bi-layer silica, two-dimensionality is explored in various materials. Amorphous silica bi-layer is a special example of a free-standing 2D material which is experimentally well studied. Another interesting bulk glass forming system is boron oxide. It may be interesting to investigate the possibility to generate 2D boron oxide in analogy to 2D-silica. Recently, a germania analogue of a silica film has been prepared in a monolayer form ref. 49 with strong substrate interaction. Investigations are ongoing to synthesize germania in a bi-layer form, which also may be a potential candidate for the application of a Yukawa-type model.

Conflicts of interest

There are no conflicts to declare.

Acknowledgements

The authors thank NRW Graduate School of Chemistry and University of Münster for providing necessary funding. We thank Markus Blank-Burian, University of Münster, for modifying the software, and providing the necessary help with coding of the simulation package. We would also like to thank Hans-Joachim Freund for his great support, as well as many of the colleagues from the Department of Chemical Physics of the Fritz-Haber-Institut whose work has been cited.

References

1 B. E. Warren, *Z. Kristallogr.*, 1933, **86**, 349–358.
2 W. H. Zachariasen, *J. Am. Chem. Soc.*, 1932, **54**, 3841.
3 L. Lichtenstein, M. Heyde and H.-J. Freund, *J. Phys. Chem. C*, 2012, **116**, 20426–20432.
4 R. J. Bell and P. Dean, *Philos. Mag.*, 1972, **25**, 1381–1398.
5 J. F. Shackelford and B. D. Brown, *J. Non-Cryst. Solids*, 1981, **44**, 379–382.
6 B. van Beest, G. Kramer and R. van Santen, *Phys. Rev. Lett.*, 1990, **64**, 1955.
7 P. Tangney and S. Scandolo, *J. Chem. Phys.*, 2002, **117**, 8898.
8 D. Herzbach, K. Binder and M. H. Müser, *J. Chem. Phys.*, 2005, **123**, 124711.
9 L. Lichtenstein, C. Büchner, B. Yang, S. Shaikhutdinov, M. Heyde, M. Sierka, R. Włodarczyk, J. Sauer and H.-J. Freund, *J. Angew. Chem. Int. Ed.*, 2012, **51**, 404–407.
10 P. Y. Huang, S. Kurasch, A. Srivastava, V. Skakalova, J. Kotakoski, A. V. Krasheninnikov, R. Hovden, Q. Mao, J. C. Meyer, J. Smet, D. A. Muller and U. Kaiser, *Nano Lett.*, 2012, **12**, 1081–1086.
11 B. Yang, W. E. Kaden, X. Yu, J. A. Boscoboinik, Y. Martynova, L. Lichtenstein, M. Heyde, M. Sterrer, R. Włodarczyk, M. Sierka, J. Sauer, S. Shaikhutdinov and H.-J. Freund, *Phys. Chem. Chem. Phys.*, 2012, **14**, 11344–11351.
12 R. Włodarczyk, M. Sierka, J. Sauer, D. Löffler, J. J. Uhlrich, X. Yu, B. Yang, I. M. N. Groot, S. Shaikhutdinov and H.-J. Freund, *Phys. Rev. B*, 2012, **85**, 085403.
13 M. Heyde, S. Shaikhutdinov and H.-J. Freund, *Chem. Phys. Lett.*, 2012, **550**, 1–7.
14 P. Y. Huang, S. Kurasch, J. S. Alden, A. Shekhawat, A. A. Alemi, P. L. McEuen, J. P. Sethna, U. Kaiser and D. A. Muller, *Science*, 2013, **342**, 224–226.
15 F. R. Eder, J. Kotakoski, U. Kaiser and J. C. Meyer, *Sci. Rep.*, 2014, **4**, 4060.
16 T. Björkman, S. Kurasch, O. Lehtinen, J. Kotakoski, O. V. Yazyev, A. Srivastava, V. Skakalova, J. H. Smet, U. Kaiser and A. V. Krasheninnikov, *Sci. Rep.*, 2013, **3**, 03482.
17 J. Horbach and W. Kob, *Phys. Rev. B: Condens. Matter Mater. Phys.*, 1999, **60**, 3169.
18 A. Saksaengwijit, J. Reinisch and A. Heuer, *Phys. Rev. Lett.*, 2004, **93**, 235701.
19 K. Vollmayr, W. Kob and K. Binder, *Phys. Rev. B: Condens. Matter Mater. Phys.*, 1996, **54**, 15808–15827.
20 R. L. C. Vink and G. T. Barkema, *Phys. Rev. B: Condens. Matter Mater. Phys.*, 2003, **67**, 245201.
21 F. Wooten, K. Winer and D. Weaire, *Phys. Rev. Lett.*, 1985, **54**, 1392–1395.
22 A. Kumar, M. Wilson and M. F. Thorpe, *J. Phys.: Condens. Matter*, 2012, **24**, 485003.
23 R. L. C. Vink, *J. Chem. Phys.*, 2014, **140**, 104509.
24 A. Kumar, D. Sherrington, M. Wilson and M. F. Thorpe, *J. Phys.: Condens. Matter*, 2014, **26**, 395401.
25 M. Wilson, A. Kumar, D. Sherrington and M. F. Thorpe, *Phys. Rev. B: Condens. Matter Mater. Phys.*, 2013, **87**, 214108.
26 J. Zhang, *Comput. Mater. Sci.*, 2018, **142**, 7–13.
27 E. Gao, B. Xie and Z. Xu, *J. Appl. Phys.*, 2016, **119**, 014301.
28 A. Malashevich, S. Ismail-Beigi and E. I. Altman, *J. Phys. Chem. C*, 2016, **120**, 26770–26781.
29 M. Heyde, G. H. Simon and L. Lichtenstein, *Phys. Status Solidi B*, 2013, **250**, 895–921.
30 J. C. Johnston, N. Kastelowitz and V. Molinero, *J. Chem. Phys.*, 2010, **133**, 154516.
31 W. Zhu, W.-H. Zhao, L. Wang, D. Yin, M. Jia, J. Yang, X. C. Zeng and L.-F. Yuan, *Phys. Chem. Chem. Phys.*, 2016, **18**, 14216–14221.
32 G. A. Méndez-Maldonado, M. González-Melchor and J. Alejandre, *J. Chem. Phys.*, 2012, **137**, 054711.
33 G. A. Méndez-Maldonado, M. González-Melchor and J. Alejandre, *Condens. Matter Phys.*, 2012, **15**, 23002.
34 S. Nosé, *J. Chem. Phys.*, 1984, **81**, 511.
35 F. H. Stillinger and T. A. Weber, *Phys. Rev. A: At., Mol., Opt. Phys.*, 1982, **25**, 978.
36 C. Büchner, P. Schlexer, L. Lichtenstein, S. Stuckenholz, M. Heyde and H.-J. Freund, *Z. Phys. Chem.*, 2014, **228**(4–5), 587–607.
37 C. Büchner, L. Liu, S. Stuckenholz, K. M. Burson, L. Lichtenstein, M. Heyde, H.-J. Gao and H.-J. Freund, *J. Non-Cryst. Solids*, 2016, **435**, 40–47.
38 D. C. Rapaport, *The art of molecular dynamics simulation*, Cambridge University Press, The Edinburgh Building, Cambridge CB2 8RU, UK, 2nd edn, 2004.

39 D. Avoav, *Metallography*, 1970, **3**, 383–390.
40 D. Weaire and N. Rivier, *Contemp. Phys.*, 1984, **25**, 59–99.
41 N. Rivier, *Physica D*, 1986, **23**, 129.
42 D. L. D. Caspar, J. Clarage, D. M. Salunke and M. Clarage, *Nature*, 1988, **332**, 659–662.
43 J. B. Clarage, T. Romo, B. K. Andrews, B. M. Pettitt and G. N. Phillips, *Proc. Natl. Acad. Sci. U. S. A.*, 1995, **92**, 3288–3292.
44 M. Mehlhorn, S. Schnur, A. Groß and K. Morgenstern, *ChemElectroChem*, 2014, **1**, 431–435.
45 S. Maier, I. Stass, T. Mitsui, P. J. Feibelman, K. Thürmer and M. Salmeron, *Phys. Rev. B: Condens. Matter Mater. Phys.*, 2012, **85**, 155434.
46 G. A. Mansoori and S. A. Rice, *Adv. Chem. Phys.*, 2014, **156**, 197–294.
47 Y. Li and D. A. Drabold, *Phys. Status Solidi B*, 2013, **250**, 1011.
48 J. Krogh-Moe, *J. Non-Cryst. Solids*, 1969, **1**, 269–284.
49 A. L. Lewandowski, P. Schlexer, C. Büchner, E. M. Davis, H. Burrall, K. M. Burson, W.-D. Schneider, M. Heyde, G. Pacchioni and H.-J. Freund, *Phys. Rev. B*, 2018, **97**, 115406.